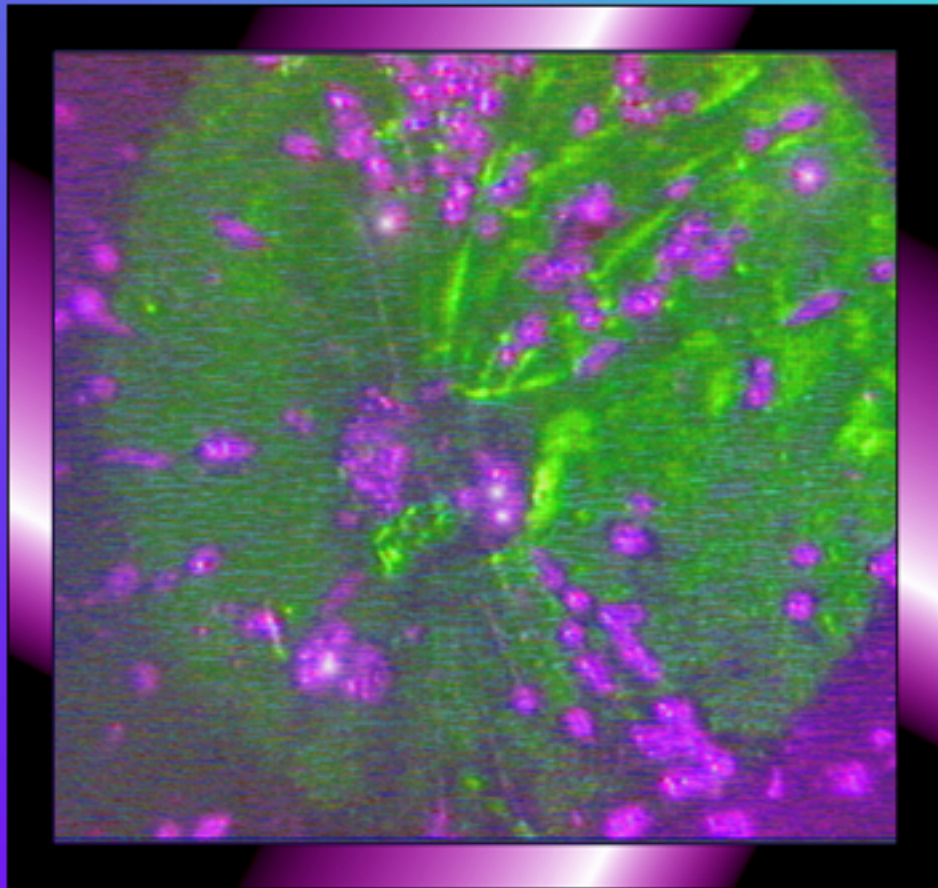


# **METALLOGRAPHIC & EXCESS ENERGY DENSITY STUDIES OF LGEN™ CATHODES SUBJECT TO A PAGD REGIME IN A VACUUM**

by

**Paulo N. Correa, M.Sc., Ph.D. & Alexandra N. Correa, HBA**



© Correa & Correa, 1992, 1993, 2001. All Rights Reserved

© Paulo N. Correa & Alexandra N. Correa 1992, 1993, 2001

All rights reserved

**METALLOGRAPHIC &  
EXCESS ENERGY DENSITY STUDIES  
OF LGEN™ CATHODES SUBJECT TO  
A PAGD REGIME IN VACUUM**

**Paulo N. Correa  
Alexandra N. Correa**

**LABOFEX Scientific Report Series, S1-007  
1992-1993**

## **CONTENTS**

<b>INTRODUCTION</b>	<b>3</b>
<b>1. Average electrode current densities</b>	<b>4</b>
<b>2. Autoelectronic emission structure, area and current densities</b>	<b>5</b>
<b>3. Low field autoelectronic emission</b>	<b>17</b>
<b>4. Pulse input energy</b>	<b>18</b>
<b>5. Reactor pulse energy</b>	<b>18</b>
<b>6. Dynamic capacitance of PAGD reactors</b>	<b>19</b>
<b>7. Anomalous reaction forces in the PAGD regime</b>	<b>19</b>
<b>8. Work-function of cathode material</b>	<b>20</b>
<b>9. Typical expected cathode lifetimes</b>	<b>21</b>
<b>10. Conclusions</b>	<b>21</b>
<b>References</b>	<b>23</b>
<b>Tables 1 to 9</b>	<b>25</b>

## **INTRODUCTION**

Supplementing the material detailed in Labofex's Scientific Reports S1-002, S1-006, and the PCT/CA93/00311 Application regarding the design of PAGD generators (LGEN™ reactors), this Scientific Report addresses the PAGD current densities at the electrodes, in the cathode PAGD plasma ball and at the emission foci. Determination of the latter two parameters required both videographic and metallographic analyses, performed utilizing diverse types of cathode metals. PAGD cathode affinity was found to correlate with the electronegativity and work-function of the metal employed, PAGD affinity increasing with decreasing work-function. Anode surface distortions were equally examined. Utilizing this data together with determinations of the pulse input energy and the energy associated with the anomalous cathode reaction forces (proportional to  $10^3$  to  $10^4$  i<sup>2</sup>) observed in the LGEN™ reactors during operation in the PAGD regime, we ascertained the fuel (cathode metal) consumption per PAGD, as well as the energy density of the fuel employed and expected cathode lifetimes.

On the basis of the results herein presented, the PAGD regime can be regarded to be an autogenous pulsatory plasma discharge regime characterized by the presence of quasi-periodic, self-generating and self-extinguishing autoelectronic cold cathode emissions that segment an abnormal plasma glow, and do so at low values of the breakdown field and at variance with the Fowler-Nordheim field-emission theory (that governs the VAD regime) with respect to the observed PAGD (low) emission current densities. Lastly, the PAGD regime deploys large anomalous reaction forces comparable to the reaction forces that have been described for water-plasma arcs, and 100x greater than those observed in VADs.

## 1. AVERAGE ELECTRODE CURRENT DENSITIES.

Following Example 5 and Table 6 of the PCT/CA93/00311 Application (1), the current densities (Table 1, columns I and M) for the overall electrode areas employed were determined experimentally and compared to the values predicted on the basis of the glow discharge theory (Table 1, columns H and L), under the same conditions and with the same devices as described for the referred Example 5. Accordingly, columns A to G are identical in Table 1 of this Report and in Table 6 of the PCT/CA93/00311 Application. As explained beforehand in Example 5 of this Application (1), given a linear factor  $k_L$  between two vacuum tubes “a” and “b”, they will have the same breakdown voltage if the pressure of “b” decreases by  $1/k_L$ , with the result that  $J$  (the average electrode current density) should decrease by  $1/k_L^2$  while  $J/p^2$  should remain constant (if the pressure varies) (2). Predicted and experimentally determined  $J/p^2$  values are shown in columns J and K of Table 1. Essentially, as the area factor between the two pulse generators is  $k_A = k_L^2$ , both the charge density  $r$  and the current density  $J$  should change by  $1/k_L^2 = 1/k_A$ , ie. inversely to the plate area factor  $k_A$ . This is indeed what is observed at breakdown ( $V_b$ ), for invariant pressure group #'s 5 and 6, columns H to K, Table 1. The same relation however does not apply as a function of the maximum input power and lowest sustaining or extinction voltages (columns L to O, Table 1), respectively, 676 and 368 V, as the plate current density and  $J/p^2$  values of the same group #'s 5 and 6 are virtually identical, despite the invariant pressure and the  $k_A = k_L^2$  area factor between the two pulse generators.

Examples of typical average electrode current densities encountered in the PAGD regime are shown in Table 2 for different area aluminum plates, as a function of the input current. Electrode  $J$  values vary from  $10^{-2}$  A/m<sup>2</sup> to  $10^3$  A/m<sup>2</sup>.

## 2. EMISSION STRUCTURE, AREA AND CURRENT DENSITIES.

Determination of the videographed equatorial diameter of the core of the cathode plasma ball at the base of each PAGD channel (see [Fig.s 1 and 2](#)) allowed us to approximate grossly the emission area per pulse and the pulse current density at the emitter surface, utilizing a reactor built with H34 aluminum plates (tube #1, Table 1 of the cited PCT application ([1](#))). Measurements were taken at the equator from the extreme infra-red light component alone of the pulsed abnormal glow discharges at fully closed aperture ([Fig. 2](#)).

At PAGD breakdown voltages ( $V_b$ ) of 1100 to 1350, the mean equatorial area of the cathode plasma globule was  $2.8 \pm 0.03 \text{ mm}^2$ . At PAGD plateau breakdown ( $V_b$ ) voltages of 700 to 850 volts, the mean equatorial area of the cathode PAGD plasma globules were 3.8 and  $0.95 \text{ mm}^2$  with anode and cathode voltages respectively (#'s 4 and 2, [Table 3](#)). As indicated by the input current progression of group #'s 2 to 5, the mean equatorial area of the cathode plasma globule increases with increasing input current (cf columns B and C, [Table 3](#)). Group #6, [Table 3](#) shows similar results for an Alzak cathode. This videographic determination of the mean equatorial area of the cathode plasma globule allowed an estimation of the overall emission, and thus the calculation of (uncorrected) emission current densities ( $J_{em}$ ), shown in column D, [Table 3](#).

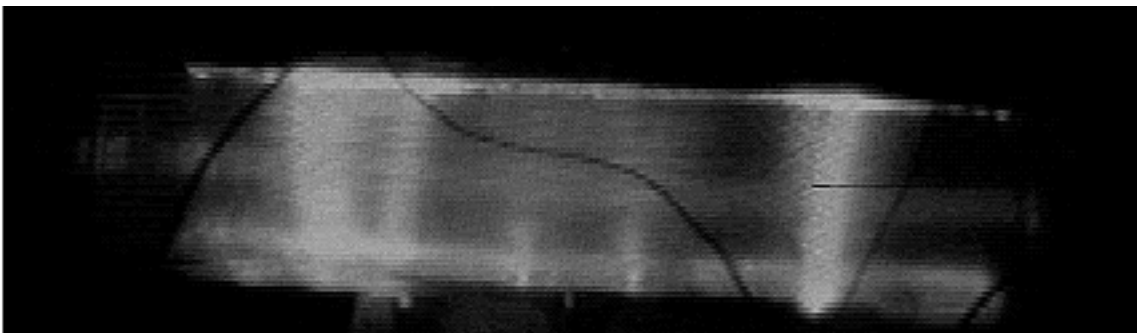


**Fig. 1-** Single video frame (31.25 msec) of 5 diachronic PAGD channels, each channel or vortex being anchored by a plasma ball at the cathode (bottom plate). LGEN™ reactor characteristics: H34 Al 128cm<sup>2</sup> area plate electrodes; 5 cm gap;  $V_b=700\text{V}$ ;  $V_x=480\text{V}$ ;  $DCA=0.24\text{A}$ ;  $ppACArms=0.6\text{A}$ ; sealed vacuum of  $10^{-6}$  Torr; 130 PPS.

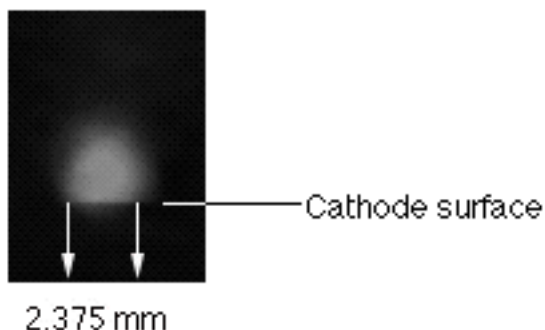


**Fig. 2-** Cathode plasma ball over the PAGD emission site in a LGEN™ reactor with Alzak plate electrodes (IR filter on). The plasma globule has a core diameter of 0.24 cm and an estimated area of 0.044 cm<sup>2</sup>. The current density at the ball's largest cross-section is  $1.25 \cdot 10^5$  A/m<sup>2</sup>. Reactor characteristics: 128cm<sup>2</sup> area plate electrodes; 5 cm gap; V<sub>b</sub>=680V; ppACArms=0.55A; sealed vacuum of 10<sup>-6</sup> Torr; 30 PPS.

Autographic analysis of the PAGD-induced cathode craters in Alzak plates was performed next, and their aspect, average inner diameter and maximal depth were determined (device #2, Table 1 of the cited PCT application (1)) after 30 seconds of operation at 500 PPS. Only isolated craters were measured, following the autograph method of Daalder (3). The PAGD operation at levels where V<sub>b</sub> and V<sub>x</sub> were very close, showed a discharge that, despite the smoothness of the surface, tended to move over most of the cathode, with the highest concentration of emission craters found at the lateral edges. The Alzak surfaces particularly lend themselves to this type of analysis because of their homogeneous aspect: before PAGD operation, the 'broken in' surface appears smooth except for very small holes (~1 to 7 μm diameter) and the 'break in' lines that appear where the Alzak was sheared during 'pulling' in at manufacture (see Fig. 3). After PAGD operation, two types and sizes of craters could be observed (see Fig.s 4 & 5):

1) the large type, or primary craters, which had an average inner diameter of  $0.28 \pm 0.03$  mm and a mean area of  $0.000615 \pm SE 7 \cdot 10^{-5}$  cm<sup>2</sup> (Fig. 4), see group # 9, Table 3;

2) smaller pits, typically distributed radially around a major crater or a cluster of these (see Fig.s 4, 5 & 6), and which have a mean diameter of 5.5 μm.

The crater complexes often occur in discrete clusters (Fig. 7) of 2 to >10, defining surface neighborhood regions of PAGD emission where the discharge repetitively struck. The inner or

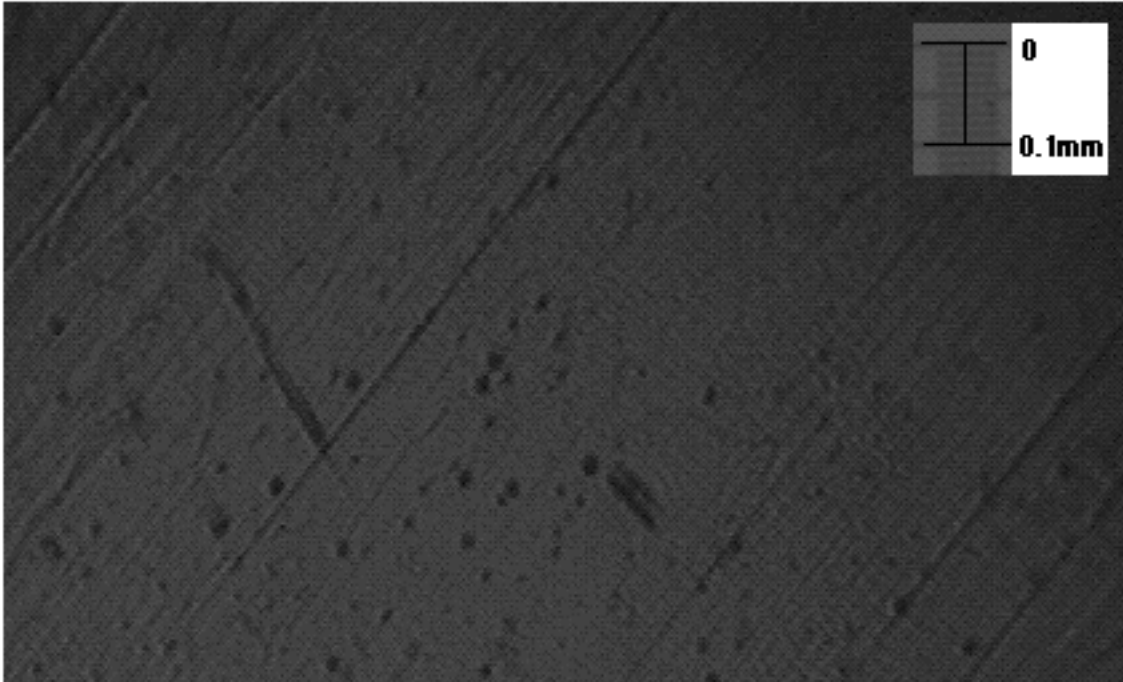


**Fig. 3-** Alzak plate surface before PAGD induction (incident transmitted light). Note the absence of crater formation or impact splatter.

bottom circular area of the primary craters characteristically shows a twirl or swirling pattern of molten metal along one of its diameters with solidified metal droplets scattered about (see Fig. 8). Gross macroscopic examination of these craters exhibits a whitish periphery suggestive of aluminum oxide deposits. The secondary craters appear to have resulted from the sputter of the primary emission site and are often found at the end of, or the intersection with, fine (0.5 to 1 $\mu$ m wide) fissure lines similar to the 'break in' lines, but distributed radially from the primary crater where they originate (see Fig.s 4 & 5); in turn, these secondary craters give way to a finer radial sputtering of their own (see Fig.s 5 and 6).

A comparison of the emission area values obtained by the autographic method of crater size determination and the videographic method of measuring the equatorial cathode ball diameter, indicates a substantial divergence between them, and the resultant estimation of the current density at the primary emission site. The reason for the discrepancy between the two methods arises directly from the emission structure encountered micrographically: even though measurements of the luminous emission globules did not include the zones of less intense luminosity (the fringe, see Fig. 1), metallographic examination had shown that each focus of emission had a multiplicity of minor emission craters associated with it; these secondary craters were dispersed in a radius of three

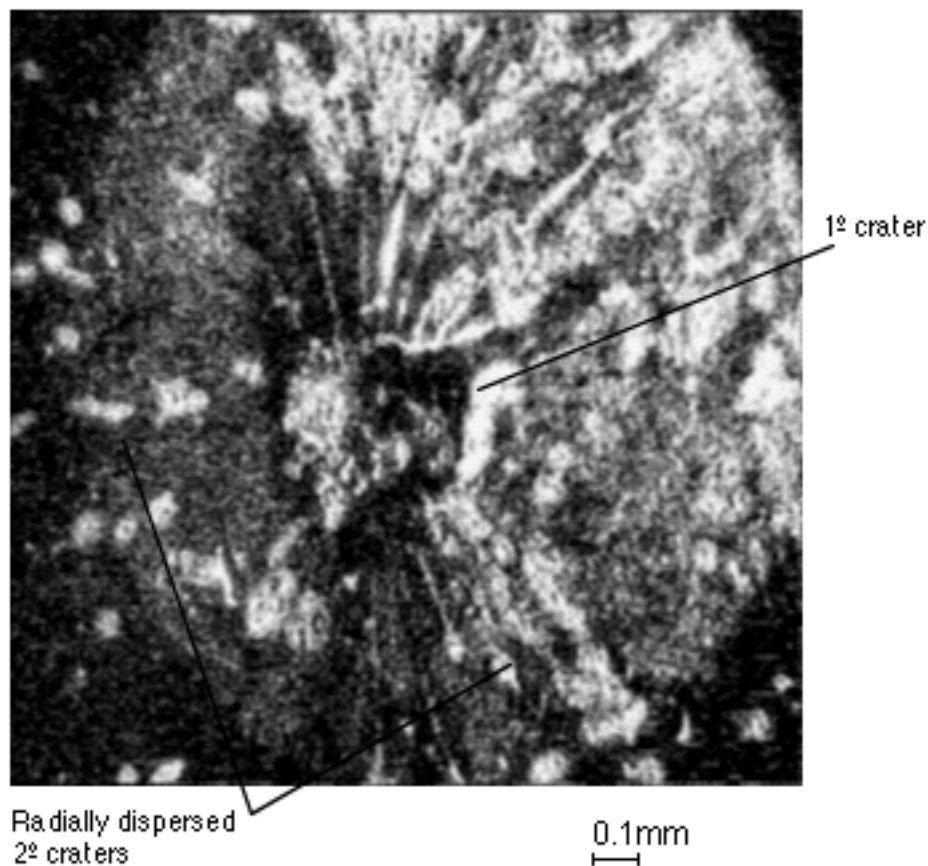


**Fig. 4-** Primary type of Alzak cathode PAGD emission crater and associated secondary pit-type craters typically found along surface crack lines radially distributed around the primary crater. Metallographic examination is performed best with a combination of incident (transmitted) and oblique light. The cathode plasma ball sits over the area of the entire complex.

to four primary crater diameters from the primary crater's center, and they thereby increased the total area involved in associated emission to an average of  $0.037 \text{ cm}^2$ . This corresponds rather well to the obtained videographic value of an area of  $0.044 \text{ cm}^2$  for the cathode plasma globules in Alzak plates, (group # 6, [Table 3](#)) as measured on the cathode that was later disassembled for autographic analysis. Typically, the videographic method overestimates the area of primary emission site by 62 to 88x. The two methods thus identify distinct structures of the emission process: whereas the metallographic method identifies primary and secondary emission sites separately, the videographic method identifies the overall area of the emission complex which includes the secondary craters associated with the primary emission site. Due to these findings, and based upon the

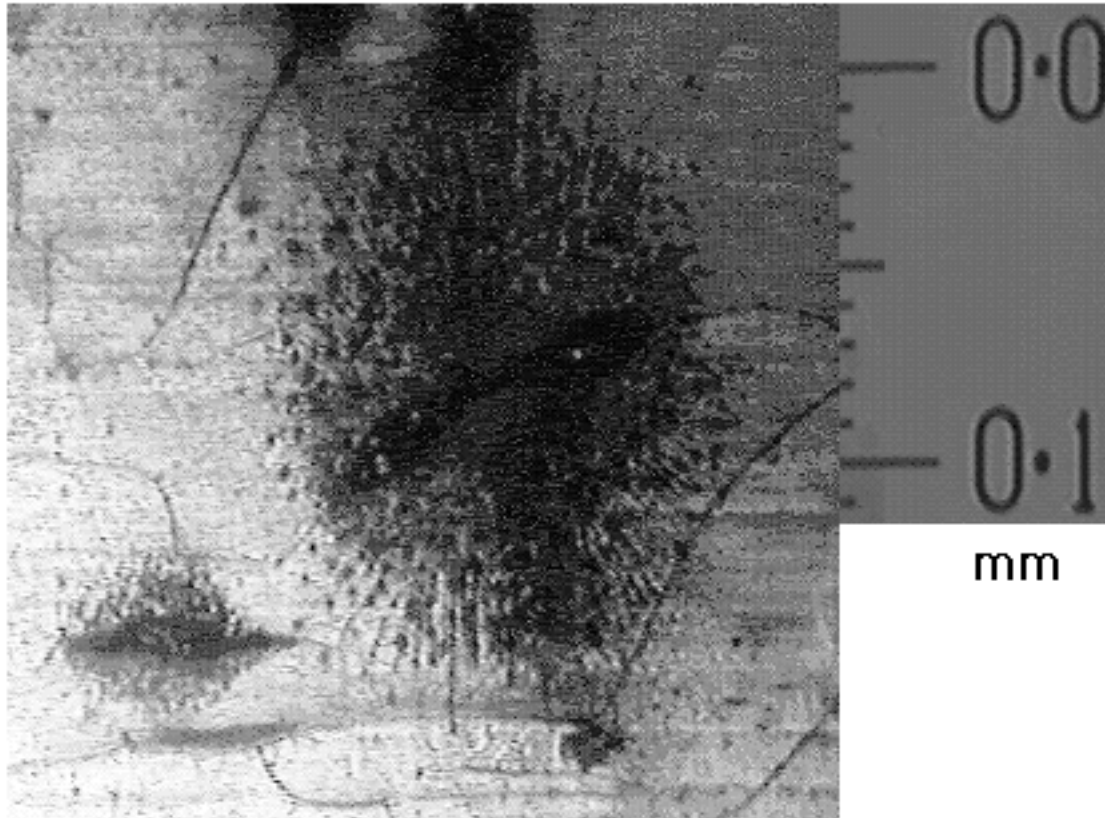


**Fig. 5-** Secondary pit-type cathode PAGD emission craters in Alzak plate electrodes (incident light). These craters radially exhibit fine lines of sputter deposition and the crack lines radiating from the primary emission site, on which they sit, are clearly visible. These pit-type craters have a sagittal inner diameter (2 to 10  $\mu\text{m}$ ) that generally is 2 to 4x smaller than their longitudinal diameter.

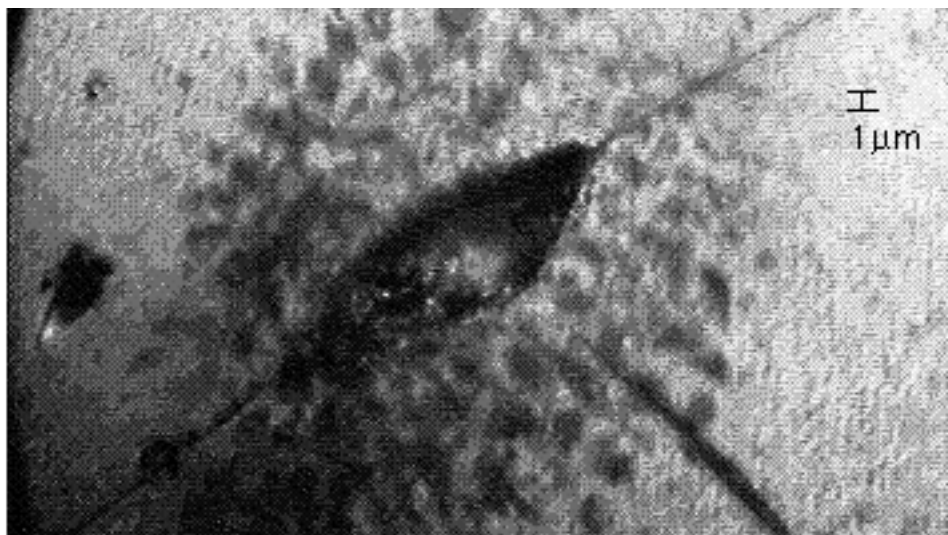


**Fig. 6-** Another example of a secondary pit-type cathode PAGD emission crater in Alzak plate electrodes (incident light, 40x apochromatic oel). The addition of immersion oil can be seen to obliterate, in a few seconds, the fine lines joining the sputter deposits to the pit.

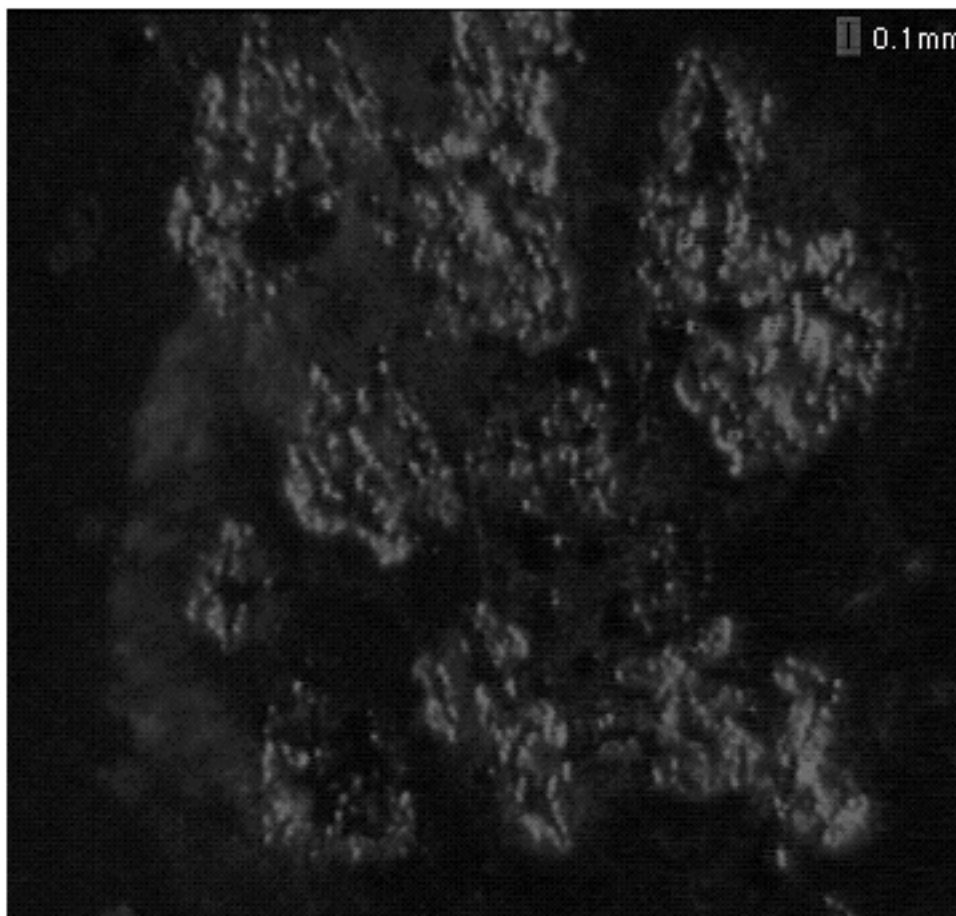


**Fig. 7-** Cluster of primary craters, associated secondary craters and scattered metal droplets on an Alzak plate surface showing a well delimited neighbourhood of PAGD emissions (incident and oblique light).

metallographic measurements, a general correction factor of 75x was applied to approximate the PAGD emission areas and current densities at the primary emission site *measured videographically*, as shown in group #'s 1 to 6, columns F to H, [Table 3](#). These values correspond *well* with the values obtained, for the same type of plate material, by the metallographic method (eg cp group # 6 with group # 9), to the advantage of the videographic method which does not require disassembly of the reactor. With this approach, PAGD primary emission site current densities as low as  $1-2.5 \times 10^5$  have been measured.

Autographic analysis of the PAGD-induced cathode craters in H34 plates was equally performed, and their average inner diameter and maximal depth were determined, examples of which are given in group #'s 7 and 8, [Table 3](#). An illustration of such a crater typically formed in isolation by high input current ( $\sim 0.4$ A DC) PAGDs, is also shown, at low and high magnification,

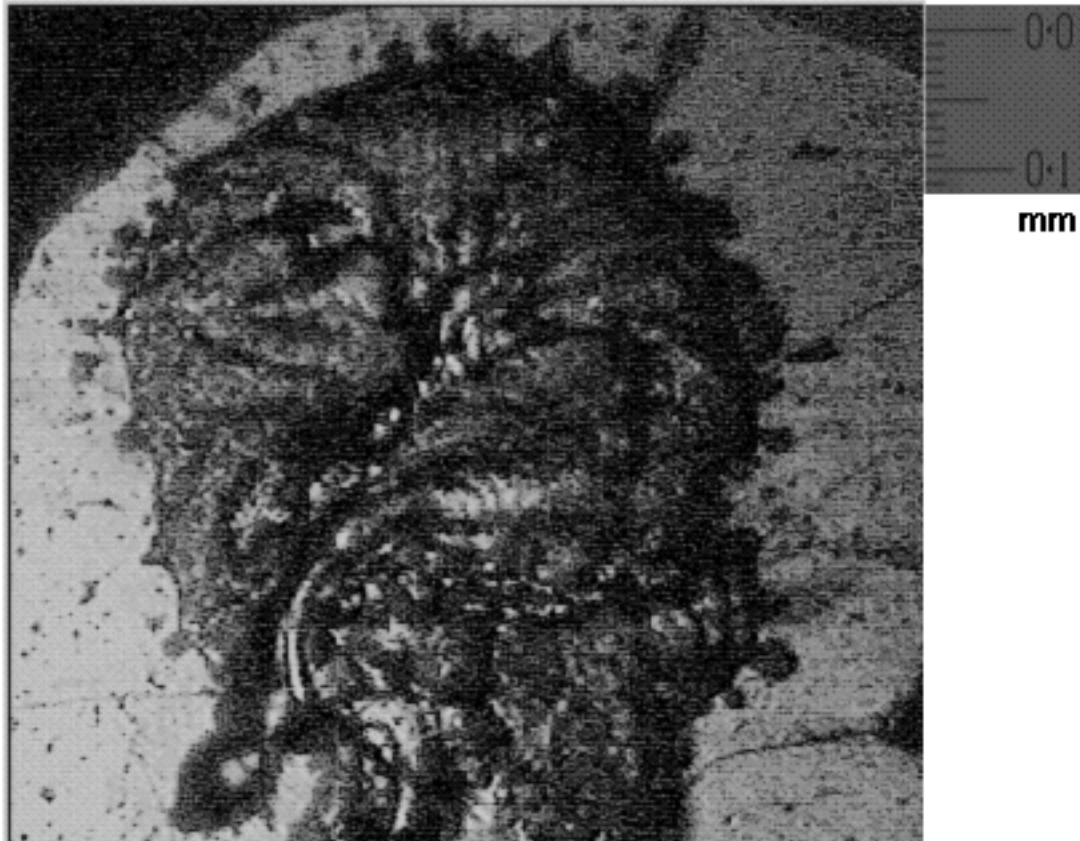


**Fig. 8-** Primary PAGD emission crater with diametric swirl pattern of molten aluminum, on an Alzak cathode (Incident and oblique light).

in Fig. 9. The secondary craters characteristically found in Alzak plates, along fracture lines irradiating from the main crater, are absent in H34 plates; instead, in H34 plates, one observes a roughened surface surrounding each crater, quite distinct from the original rough aspect of the pulled finish of these hardened aluminum plates, as if the surface surrounding the emission crater was boiled off. Like the Alzak-PAGD primary craters, the aspect of the H34-PAGD emission craters is a concave one, having raised circular borders (the lip), somewhat like a volcano. This topology may be easily seen in differential interference contrast emulations shown in the micrographs of Fig.s 10 and 11. Often, at the bottom of the concavity, the H34 craters have a convex, cooled molten metal droplet. Eventually, as the pitting resulting from PAGD cathodic emissions covers the entire cathode, the cathode surface gains a very different aspect from the original one (Fig. 12), as it becomes finely pitted with interspersed protuberances. In this process, craters from earlier metal layers become progressively covered and eroded by subsequent emissions from the same cathode, as shown in Fig. 13.

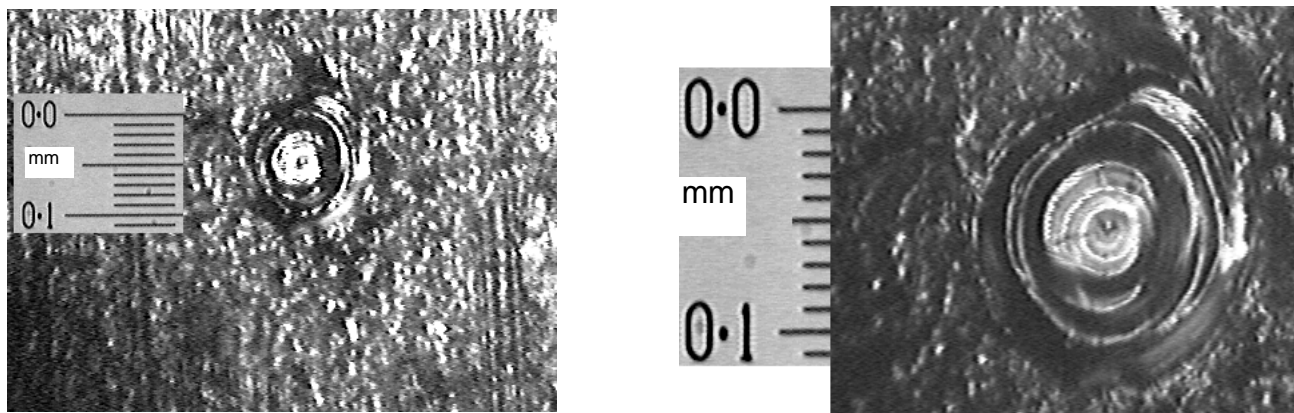


**Fig. 9-** Low (on the left) and high (on the right) power micrographs of a single, typically isolated, primary PAGD emission crater in a H34 Al cathode plate (incident and oblique light). The core of these craters is hollowed out (concave core) and is often occupied by a convex molten metal droplet or spherule. On the left micrograph, one can observe a profusion of surface distortions surrounding the crater, which probably arose from the 'fall out' of material ejected by the explosive emission mechanism responsible for primary crater formation. From videographic analysis, the cathode plasma ball sits over the entire area occupied by the primary crater and the surrounding 'boiled off' periphery.

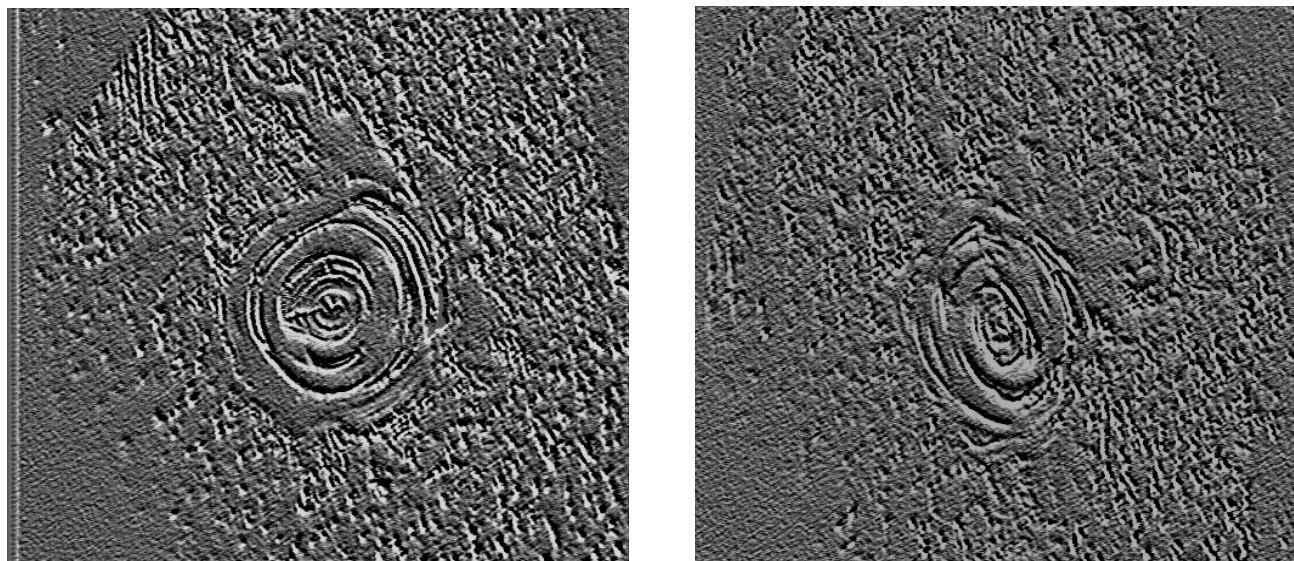


**Fig.s 10 (Left) & 11 (Right)-** Digitally processed differential interference contrast emulations of actual micrographs for PAGD emission craters in H34 Al plate electrodes. The 'boiled off' periphery is clearly visible as a ring of protuberances surrounding the raised lip of the crater; the core of the crater is hollowed out, and the embossed spiraloid imprint of the entire formation (lips plus concave core) indicates that the tip of the PAGD channel where the cathode plasma ball sits, is the apex of a vortex that burrows into the cathode surface. It also suggests that the entire PAGD channel has an associated spin. Actual magnification:~150x.

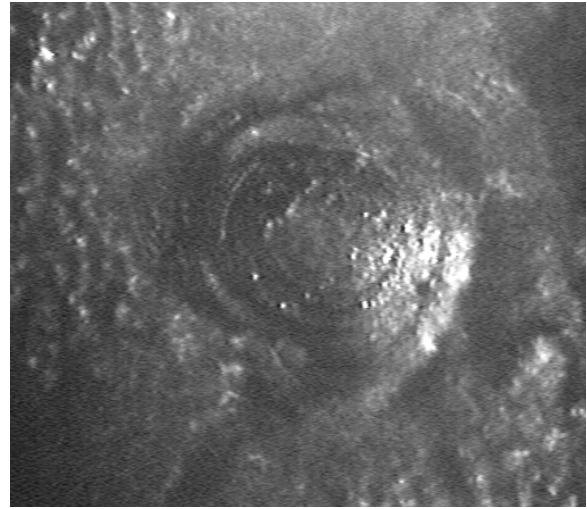
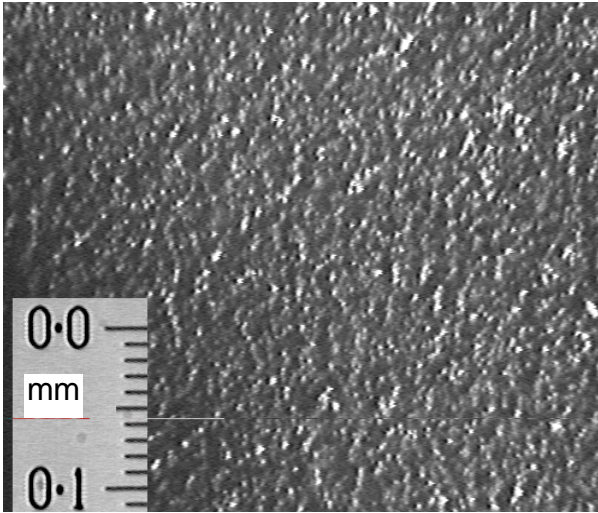


**Fig.s 12 (Left) & 13 (Right)-** Left: Aspect of a H34 Al cathode surface being continuously pitted, eroded and covered by the 'boiling off' effect of multiple PAGD emission craters and their sediments. Right: A PAGD emission crater in a H34 cathode, in the process of being eroded and re-covered by the peripheral distortion adjacent to neighbouring craters (200x mag).

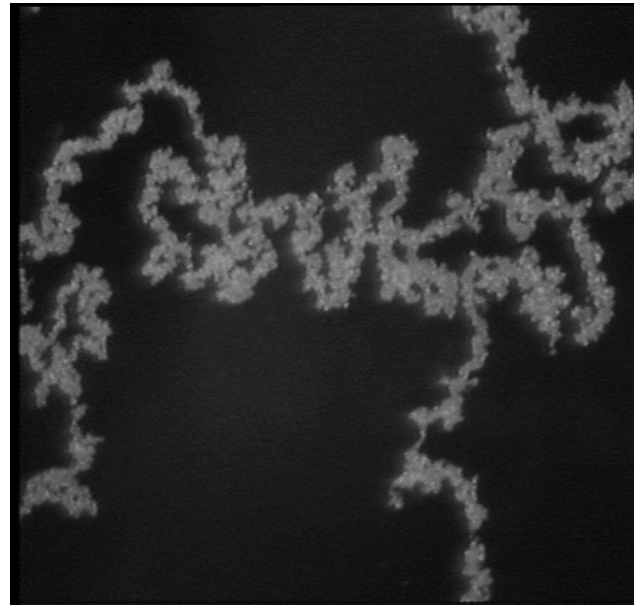
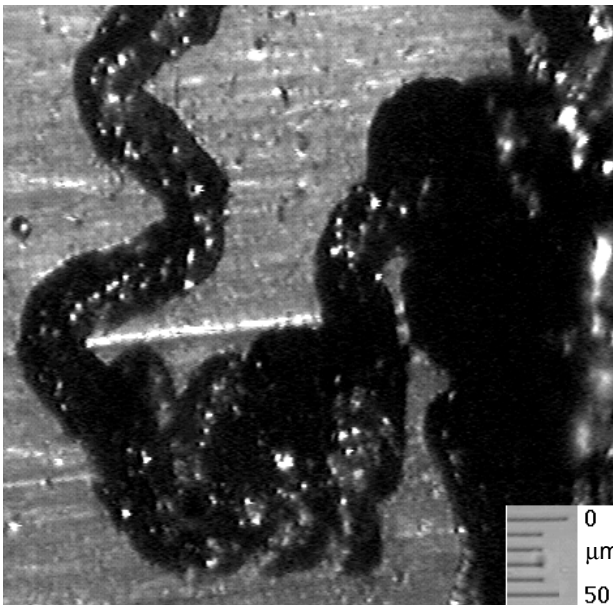


**Fig.s 14 (Left) & 15 (Right)-** Cathode itinerant sinusoidal track signatures on an Alzak plate surface (**on the Left**) and on a semi-cylindrical silver-plated cathode (**on the Right**), due to high frequency auto-electronic PAGD emissions at high input current (1.8A on the left) occurring centered around a single event, or to evenly spaced high frequency PAGD emissions at lower input current (0.2A on the right), on highly polished surfaces. Itinerant tracks akin to Rakhovsky Type II cathode spots, appear to be a PAGD track signature at high frequency of auto-electronic emission *in highly mirrored cathode surfaces*. These signatures occur in boundary conditions close to those that will elicit a full-fledged VAD regime. The sinusoidal patterns observed also suggest that they are the result of the spin of the discharge cone, with its wobbling signature similar to that of a spinning top.

These PAGD crater signatures are akin to Rakhovsky Type I VAD cathode spots (4), of discontinuous manifestation and far from steady state, except they occur at very low fields and with low emission current densities (see below). However, itinerant track signatures akin to those described by Rakhovsky for Type II VAD cathode spots may also be observed at high PAGD frequencies of autoelectronic emission, be this high-frequency due to high input currents and their clustering of multiple emissions and plasma re-ignitions around a single event (see Fig. 14), or be it due to fast, periodic autoelectronic emissions and plasma re-ignitions evenly spaced apart in time and at lower input currents (see Fig. 15), *on highly polished cold cathode surfaces*. It is probable that the PAGD cathode crater formation observed is a low PAGD frequency and moderate input current phenomenon. In highly polished aluminum surfaces, this PAGD cathode ejection phenomenon is accompanied by formation of radial, zig-zagging crack lines where other secondary emission sites originate. In hardened aluminum cathode surfaces that have a smooth finish, the PAGD emission sites splay out from a central zone in patterns reminiscent of Mandelbrot's fractals, branching out along the crack lines. This is clearly seen in Figs 16 and 17, where the starry emission sites are very shallow and do not present a crater, the central zone of the emission being characterized by the concentration of spikes and cooled metal droplets. Similar fractal patterns are observed in highly polished aluminum surfaces, such as Alzak, not as the result of a single emission site, but, as shown in Fig. 14, as the result of successive emission sites, as if the PAGD emission foci were burrowing a furrow on the surface of the cathode. Possibly, at higher input currents or high rates of PAGD auto-electronic emission, one or more of the crack lines joining the secondary sites becomes a track for successive primary emission foci (volcanic action model), with the result that the discharge preferentially migrates along one of these fissure lines, which it keeps on repeatedly creating as it moves forward, to produce furrows of itinerant emission. Like the path of a micro-cyclone, the resulting track has a sinusoidal appearance. Together with the spiraloid imprint at the emission crater (the helicoidal lip and the helicoidal burrowing of the crater core), this suggests that there is a net spin associated with the plasma vortex at the cathode, and thus that the cathode plasma ball exhibits gyration. It also suggests that the underlying spin field is transmitted across the separate and successive emission events and respective cathode plasma balls, to form the spiraling track signatures.

Altogether different is the surface deposition process occurring at the anode; here, the surface appears to become more uniform, through the mirroring and possibly abrasive actions of the cathode jets. Macroscopically, with time of PAGD operation, the anode surface appears cleaner and polished. However, with the most intense PAGD discharges, one can observe the formation of diverse size (from ~25 to 500 $\mu$ m widest diameter) molten metal bubbles, often with a smeared aspect (splatter type), ringed all the way around by a concave or inverse lip, like a moat, on the anode surface of both H34 and Alzak electrodes (see Figs 18 and 19). As shown in the diagram of

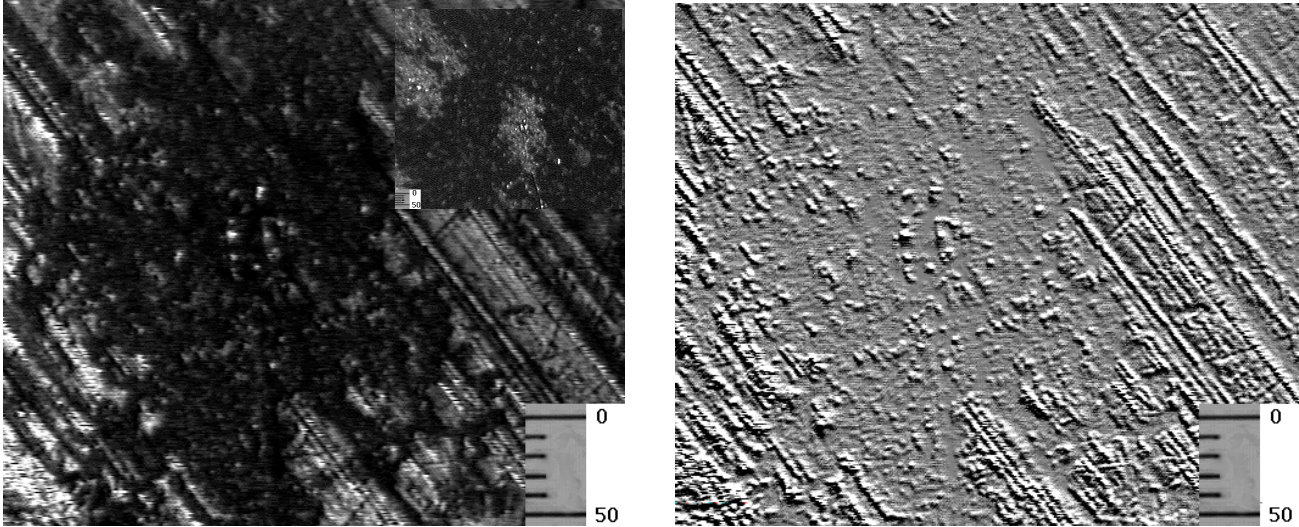


**Fig.s 16 (Left) & 17 (Right)-** High power micrographs of a spread-out PAGD emission crater in hardened aluminum plates, lacking a distinct central crater and generally with a shallow concavity (incident and oblique light). Inset (incident light) shows the same emission site and two other neighbouring ones. Differential interference contrast emulation of Fig. 16 is shown on the right (Fig. 17). The central zone is merely marked by the cluster of protrusions and droplets. DCA input: 0.6A.

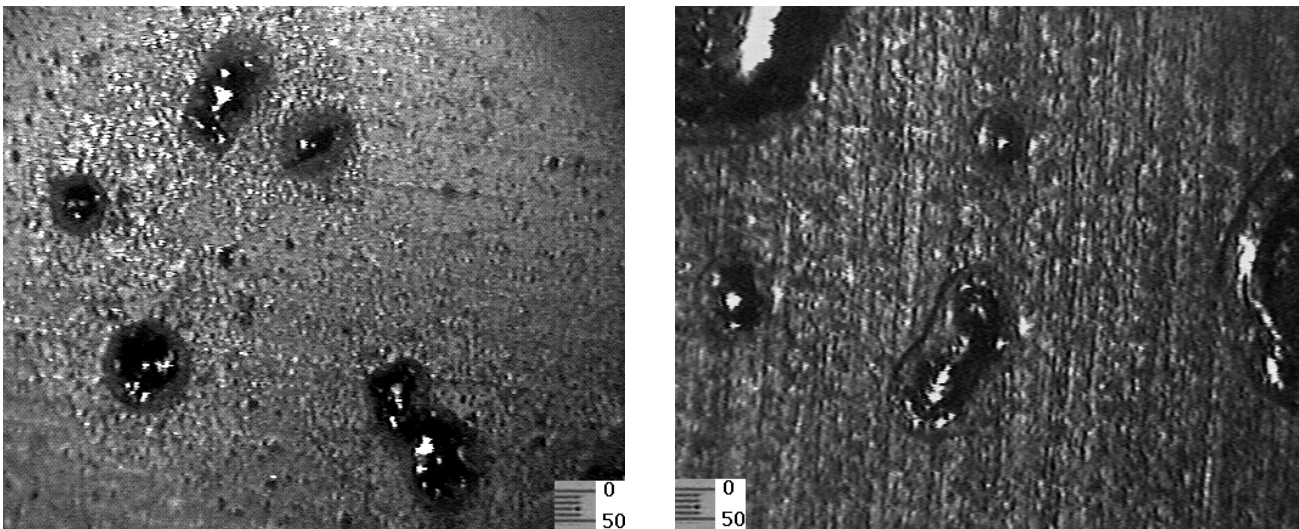


**Fig.s 18 (Left) & 19 (Right)-** Micrographs of splattered molten metal on the anode surface of Alzak, **on the Left**, and H34 Al electrodes, **on the Right**. These mound formations are due to the impact of very fast plasma metal ions (ion stream from the cathode) that deposit on the anode and punctually heat up its surface to form convex metal bubbles (local melting) surrounded by a concave border.

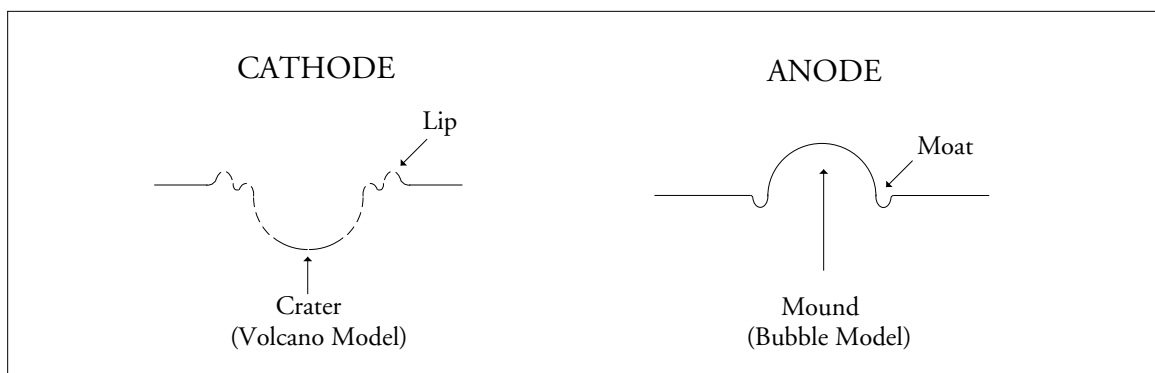


**Fig. 20-** Diagram of the outline of a cross section through cathode PAGD primary emission craters, on the left, and anode molten bubbles, on the right, showing their negative aspect (lips and concavity in the former, moat and convex formation in the latter).

Fig. 20, these anode signatures are the inverse or negative form of the cathode craters observed under the same conditions of PAGD operation. This is seen to further corroborate the cathode emission mechanism discussed (ejection of metal ions) and the collection of the plasma metal ions, by impact, at the anode.

With the data obtained by the metallographic method of crater measurement, we estimated the volume of metal ejected from a H34 Al cathode, by assuming that the crater represents a concavity analogous to a spherical segment having a single base ( $1/6\pi * H [3r^2 + H^2]$ , where H is the height of the spherical segment and r the radius of the sphere), while disregarding the volume of the occasional central droplet leftover from the emission. The following are mean  $\pm$ SEM crater diameters (D), crater depths (H) and volumes (V) of extruded metallic material for two types of aluminum cathodes, Alzak and H34 hardened aluminum, subject to a high input current PAGD:

- 1- Alzak: D-0.028cm $\pm$ 0.003; H-0.002cm $\pm$ 0.0002; V- 6.2\*10<sup>-7</sup>cm<sup>3</sup>;
- 2- H34: D-0.0115cm $\pm$ 0.0004; H-0.0006 $\pm$ 0.0001; V- 3.1\*10<sup>-8</sup>cm<sup>3</sup>;

This data indicates that, on the basis of the input currents, the PAGD reactors do not reach the critical value of  $\sim 7 * 10^8$  A/m<sup>2</sup>, ie the threshold required by the Fowler-Nordheim theory for field emission. How is emission occurring at low applied fields and low emission current densities? Based on measurements of the peak pulse current developed by the reactor, there is an anomalous reaction current set up within the reactor. This is exemplified in Fig. 18 B of the PCT/CA93/00311 Application (1). These anomalous reaction currents may be as low as 100 mA but, typically of interest, are of the order of 0.5 to >200 A. On the basis of this anomalous reaction current

phenomenon, primary emission current densities of the order of  $10^7$  to  $10^9$  A/m<sup>2</sup> can be estimated.

### **3. LOW FIELD EMISSION**

Unlike prior art planar or coaxial electrode discharge devices (5-8), which utilizes short gap and high field discharges (typically >100,000 V/m) in the absence of an unexploited electrode area effect, the PAGD reactors are essentially low breakdown field devices with long gaps, and which advantageously employ the area effect to reduce the field strength, as described previously for Fig. 11 of the PCT/CA93/00311 Application (1). Typical examples of the values of the PAGD breakdown fields at various negative pressures, for aluminum and nickel cathodes of reactors that were sealed (at diffusion pump vacua) or pumped down (by rotary pump action), are shown in Table 4. The breakdown field values mostly range from 5,000 to ~30,000 V/m. Similar ranges were shown in Fig. 11 of the PCT/CA93/00311 Application, where PAGD breakdown fields can be seen to vary from a minimum of 2,730-5,090 V/m to a maximum of 15,640 V/m. (Extinction field values may be as low as 1,000 to 2,000 V/m.) As extensively discussed in the referred to PCT application, the breakdown field value is modulated by the voltage reduction area effect, the interelectrode gap distance and the residual gas pressure in the gap. Generally, increasing the gap distance increases the required field strength. The voltage reduction effect of large area electrodes appears to be mainly responsible for the low field breakdown characteristics of the self-generating auto-electronic emissions encountered in the PAGD regime. Field-emission theory typically requires a very high breakdown field value, greater than  $2 \times 10^9$  V/m, for auto-electronic emission (eg in a VAD). If we disregard momentarily the fact that the PAGD has a positive  $I/V^2$  slope and take its cathode- or anode-supplied voltage intercepts in a Fowler-Nordheim plot (0.0005 and 0.00005, respectively) to calculate the field-enhancement factor  $\beta$  required by the field-emission theory to explain the unpredicted auto-electronic emissions observed in the PAGD regime, we end up with  $\beta$  values of the order of  $10^6$  to  $10^7$  (for actual fields of 15,000 V/m), if we are to assume (which we should not) that the long gap PAGD operates like a (short-gap) VAD. Indeed, what is remarkable about the PAGD regime in these reactors is the very low (> $10^5$ -fold lower) values of the fields required for the PAGD transduction of high current densities, a phenomenon that actually occurs in known VAD regimes (cold cathode or thermionic), but typically at  $10^2$ -fold lower values than those required and predicted by the field-emission theory (9).

#### 4. PULSE INPUT ENERGY.

Pulse input energy was determined for a variety of conditions (pressure, gap, electrode area, residual gas, input current and input voltage, duration of input pulse, cathode material, etc) and typical examples are presented in [Table 5](#). In the PAGD regime, input pulse duration and corresponding duty cycle are self-regulated events dependent upon the frequency controlling factors discussed in the PCT/CA93/00311 Application (1), and thus the input pulse times shown in [Table 5](#) are spontaneous and not externally determined, eg as for interrupted vacuum-arc discharges (IVADs). As a function of the input power characteristics, input energy per pulse in the PAGD regime ranged from as low as 1 mJ to >112J ([Table 5](#)). Values as high as 250J/PAGD input energy have been determined without slippage to a VAD regime for typical 5-8 cm gap, 4 to 128 cm<sup>2</sup> plate reactors. Under the same conditions, higher values will promote slippage of the PAGD into the VAD regime. However, higher values are possible with still longer gap reactors and higher input currents (eg 4 to 10 A).

#### 5. REACTOR PULSE ENERGY.

Typical input, reactor and output energies per pulse, respectively, columns A to C, ordered vertically by increasing input energy, are shown in [Table 6](#). The data was obtained with plate reactors of 4 to 128 cm<sup>2</sup> cathode areas, gaps of 5 to 8 cm, at different pressures (in air or argon) and PPS rates of 0.1 to 110 (column D, [Table 6](#)). Two separate types of associated circuits were utilized to measure the output energy per pulse (column C, [Table 6](#)):

1) In a double diode configuration, oscillographic reactor measurements for groups # 1 to 3, [Table 6](#), were taken at the junctions of the cathodes with capacitors 10a and 10b (Fig. 21A of the PCT/CA93/00311 Application (1)), and at the junction of the axial anode with another capacitor placed prior to the centertap of transformer 26, in series with both parallel capacitors 10a and 10b. Coils 26a and 26b of transformer 26 were replaced by a third series capacitor intermediate parallel capacitors 10a and 10b, and oscillographic AC output readings taken across this capacitor (groups # 1 to 3, [Table 6](#)); the total series capacitance was 5.3  $\mu$ F.

2) In a single diode configuration, oscillographic reactor measurements for groups # 4 to 14,

Table 6, were taken at the junctions of the cathode with capacitor C3, and of the anode with capacitor C5 (Figs 23 and 38 of the Energy Conversion System PCT/CA93/00430 Application (10)), and oscillographic or long-term DC output readings were determined at the input to the battery pack CP (Figs 23 and 38 of the Energy Conversion System PCT Application (10)); the C3/C5 series capacitance was 17.5mF.

Two conclusions, independently from all other varying conditions, may be taken from Table 6 data: the pulse energy released within the reactor varies from <3 to >50x the input energy per pulse (column A vs columns B and C); and, in general, the reactor energy varies inversely to the pulse frequency (columns B and C, vs column D). In other experiments, reactor energies per pulse have been observed to reach >500J. Given that the reactor pulse voltage ( $V_p$ ) is determined by the extinction voltage  $V_x$  ( $V_p = V_b - V_x$ ) and thus cannot reach the amplitude of the breakdown voltage  $V_b$ , this involution of energy observed per pulse in the reactor and at its output indicates that it is a current amplification phenomenon. Indeed, with input currents of 1.2 to 1.7A and input pulse energies of 1 to 30J, peak pulse reactor currents have been observed to reach >150A.

## **6. DYNAMIC CAPACITANCE OF PAGD REACTORS**

We have previously reported the calculated static capacitance of typical plate area reactors (p.43, lines 19 to 21). A typical 128 cm<sup>2</sup> plate reactor would have a capacitance of the order of 2 pF, and at an applied 560V potential, be capable of storing 0.3 micro-Joules, an infinitesimal quantity of energy ( $E = 0.5 C V^2$ , where E is in Joules, C in Farads and V in Volts). With a typical pulse input energy injection of 5 to 15 J, the reactor will develop 25 to >400 J per pulse; at pulse reactor voltages ( $V_p$ ) of 100 to 500, the dynamic capacitance of the discharge tube will range from 0.2 to 80 mF.

## **7. ANOMALOUS REACTION FORCES IN THE PAGD REGIME**

Determinations of the anomalous cathode reaction forces in the PAGD regime was carried out utilizing the reactor pulse energy or the pulse output energy, together with the metallographic data or by measuring the force in a reaction balance. The kinetic energy of each pulse was determined either directly, by integration of oscilloscopic pulse profiles, or indirectly, by long-term resistive discharge measurements of the batteries storing output power. The cathode material utilized for these experiments had a density of 1.86 g/cm<sup>3</sup>. For a mean net pulse output energy of 86.4 J (Net energy out=input reactor energy - output reactor energy), or 24 mWh, and a mean

volume of cathode metal ejected of the order of  $3.1 \cdot 10^{-8} \text{ cm}^3$ , a single PAGD releases  $5.8 \cdot 10^{-8} \text{ g}$  of metal in 40 to 50 msec, or  $1.3 \cdot 10^{15}$  Al ions. Accordingly, the calculated kinetic energy of each Al ion leaving the cathode is quite high, of the order of  $4.8 \cdot 10^5 \text{ eV}$ , more than three orders of magnitude greater than that typically found in VADs (11-13). Under these conditions of PAGD production and measurement, the energy density of the Al cathode being operated in a PAGD reactor, is of the order of  $2.8 \cdot 10^9 \text{ J/cm}^3$ , only three orders of magnitude less than the energy density value of the energy priming the vacuum, as calculated by Aspden (14). Corresponding rms vapor velocity of the ejected Al ions was  $1.7 \cdot 10^8 \text{ cm/sec}$ . Utilizing Tanberg's formula for the reaction force  $F_R$  in dynes ( $F_R = m \cdot V / 1.39$ ), such a typical PAGD deploys an anomalous reaction force of 143.6 dynes. Determination of the anomalous ion force by reaction weight measurement, under similar conditions, yielded 245.2 dynes. Anomalous cathode reaction forces  $>300$  dynes have been observed in other PAGD experiments (with pulse output energies of 25 to  $>100 \text{ mWh}$ ).

In referring to the anomalous reaction forces present in VADs (Tanberg's and Kobel's work), Aspden has suggested a proportionality of the order of  $100 \cdot i^2$  (where  $i$  is input current in real units), for the electrodynamic action observed in these experiments (15). Graneau et al (16-17), in their calculation of the average acceleration force for water-plasma arcs ( $F_{av} = \mu_o / 4\pi (k \cdot i^2)$ , where  $\mu_o$  is the permeability constant of the vacuum in Henrys per meter, and the force is in Newtons) have utilized  $k$  as a figure of merit for the strength of the explosions observed. As may be seen from Table 7, the  $k$  values of the PAGD are very high (100x higher than those observed in VAD studies, cp VAD groups # 1 to 3 with PAGD groups # 6 and 7, Table 7), and comparable to those calculated by Graneau et al for water-plasma arc explosions. Yet, the PAGD input current values are the lowest of all groups. Following Aspden's interpretation of the law of electrodynamic action, the PAGD  $k$  values are found to be in the range prescribed by the ion/electron mass differential for Al ions (49,185), which lies in the  $10^4$  range.

## 8. WORK-FUNCTION OF CATHODE MATERIAL

Based upon data for the PAGD performance of diverse cathode materials presented in the PCT/CA93/00311 Application, together with Pauling's tabulation of element electronegativities (Electronegativity  $X = 0.44\phi - 0.15$ , where  $\phi$  is the work-function of the element (18), we determined the PAGD affinity of diverse cathodes to decrease with increasing element electronegativity ( $X$ ) and cathode work-function ( $\phi$ ), as shown in Table 8. The lower the work-function of the cathode metal utilized, the greater was the observed PAGD affinity. It is expected that materials with work-functions of  $<1.5$  (and lower electronegativities), such as Li, Be, Mg, Cs, etc, will support PAGD production like Al does, or better. The only cathode material tested not in plates but in thin rods was

tungsten (W). No correlation of PAGD production affinity with any of the other physical parameters considered (eg atomic electron affinities, ionization potentials, atomic weight, density, melting and boiling points, thermal conductivity and electrical resistivity) was found, except that the two best PAGD cathode emitters had the lowest melting points and densities of all cathodes examined.

## **9. TYPICAL EXPECTED CATHODE LIFETIMES.**

Accordingly, utilizing plates composed of either material with 3mm of thickness, and thus with a volume of 38.4cm<sup>3</sup> per plate and considering that only 2/3rds of the cathode shall be used (a 2mm layer out of the 3mm thickness), the total number of pulses per plate total (TLT) and partial (PLT) lifetimes is theoretically:

- 1- Alzak:        TLT: 6.2\*10<sup>7</sup> pulses; PLT: 4.1\*10<sup>7</sup> pulses;
- 2- H34:        TLT: 1.2 \*10<sup>9</sup> pulses; PLT: 8.1\*10<sup>8</sup> pulses;

Typically, a H34 device can produce ~0.25kWh per 10,000 pulses. The corresponding value for a PLT is thus a minimum of 1.0MWh/Alzak cathode and of 20MWh/H34 cathode. As the cathode for each combination is only 66.7% consumed, the vacuum pulse generator may continue to be used in a reverse configuration, by utilizing the other plate in turn as the cathode; thus, the minimal values become, respectively, 2.0MWh/Alzak pulse generator and 40MWh/H34 pulse generator. The same rationale applies if the configuration utilized was that of the double diode.

## **10. CONCLUSIONS**

A summary of the typical specifications of PAGD reactors is presented in [Table 9](#), though its values should not be construed as limits to the phenomenon such as it might manifest itself in other conditions.

Unlike other discharge tubes in prior art ([5-8, 19](#)), which must be triggered by an external pulse generator, the PAGD reactor is the oscillator component in any of the pulse generator circuits discussed in the PCT/CA93/00311 Application ([1](#)). Essentially, the PAGD reactor is a low breakdown field oscillator that does not require a trigger electrode, nor any external shaping of the applied current or voltage, which is simply DC. In distinction from the externally pulsed abnormal glow discharge described by Manuel's patent ([19](#)), the PAGD regime is a self-pulsed or self-

generated, and self-regulated discharge method. In fact, with the appropriate input resistance, a PAGD reactor as described, will operate in the PAGD regime autogenously, in the absence of any parallel capacitance, and utilizing solely a battery pack as a power source. The PCT/CA93/00311 Application in fact describes the physical and operational parameters necessary to configure a vacuum discharge tube to elicit self-generating discharges, and thus be self-pulsed, in the PAGD plasma regime, directly from a direct current supply.

Unlike prior art glow discharge tubes that are fundamentally flash over devices that do not employ any form of emission (6, 19), the discharge has both a glow and an (autoelectronic) emission component. Unlike VAD tubes (5,7), the cold cathode PAGD autoelectronic emission pulse is not triggered externally, but a spontaneous occurrence observed at low breakdown fields, with emitter current densities 10 to 1000x lower than those required by the Fowler-Nordheim theory for field emission.

As observed in prior art VAD devices (eg Tanberg's or Kobel's cited work), anomalous cathode reaction forces are set up in the PAGD reactors; however, with 10 to 100x lower input currents than needed for a VAD, the PAGD-associated reaction forces manifest a proportionality constant that is 10 to 100x higher than found for VADS ( $10^3$  to  $10^4 \cdot i^2$  vs  $10^2 \cdot i^2$ ). We think that these forces may account for the low input current densities observed in the PAGD regime. Evidently, as with the PAGD regime itself, these reaction forces result from the specific physical and operational parameters employed, amongst which the large gaps, large electrode areas, cold cathode status, low breakdown fields and cathode low work function figure prominently.

## REFERENCES

1. Correa, PN & Correa, AN, (1993) "Pulse Generator (2)", PCT application.
2. Gewartowski, JW & Watson, HA (1957) "Principles of Electron Tubes", D. Van Nostrand Co., Inc, NY, NY, pp. 545-550.
3. Daalder, JE (1974) "Diameter and current density of single and multiple cathode discharges in vacuum", IEEE Trans Power Appar Syst, PAS-93:1747.
4. Harris, LP (1980) "Arc cathode phenomena", in "Vacuum arcs, theory and application", Lafferty, JM, Ed., J. Wiley & Sons, NY, NY, p.120 & f.
5. Boetcher, GE (1972) "Cold cathode vacuum discharge tube with cathode discharge face parallel with anode", U.S.P.# 3,663,855.
6. Conrad, JR (1988) "Method and apparatus for plasma source ion implantation", U.S.P. # 4,764,394.
7. Alexandrovich, E et al (1974) "Flash X-ray tube", U.S.P. # 3,821,580.
8. Dethlefsen, R (1992) "Coaxial pseudospark discharge switch", U.S.P. # 5,126,638.
9. Farrall, GA (1980) "Electrical breakdown in vacuum", in "Vacuum arcs, theory and application", Lafferty, JM, Ed., J. Wiley & Sons, NY, NY, p. 20 & f.
10. Correa, PN & Correa, AN, (1993) "Energy Conversion System", PCT application.
11. Tanberg, R (1930) "On the cathode of an arc drawn in vacuum", Phys Rev, 35:1080.
12. Kobel, E (1930) "Pressure and high vapour jets at the cathodes of a mercury vacuum arc", Phys Rev, 36:707.
13. Plyutto, AA et al (1965) "High speed plasma streams in vacuum arcs", Sov Phys J Exp Theor Phys, 20:328.
14. Aspden, H (1975) "Gravitation", Sabberton Publications, Southampton, UK, p.61.
15. Aspden, H (1969) "The law of electrodynamics", J Franklin Inst, 287:197.
16. Graneau, P & Graneau, PN (1985) "Electrodynamic explosions in liquids", Appl Phys Lett, 46:470.
17. Azevedo, R et al (1986) "Powerful water-plasma explosions", Phys Lett A, 117:101
18. Lange's Handbook of Chemistry", 1979, McGraw-Hill Book Co, NY, NY, p.3-11.
19. Manuel, E (1969) "Method of forming a flexible organic layer on metal by a pulsed electrical abnormal glow discharge", U.S.P. # 3,471,316.

# **TABLES**

TABLE 1

No.	<u>A</u> W (cm)	<u>B</u> L (cm)	<u>C</u> Plate (K <sub>L</sub> )	<u>D</u> Area (cm <sup>2</sup> )	<u>E</u> K <sub>A</sub>	<u>F</u> d (cm)	<u>G</u> p (Torr)		
1	16	4	1	64	1	3.6	2.8 * 10 <sup>6</sup>		
2	32	4	1.41	128	2	5	2.0 * 10 <sup>6</sup>		
3	32	8	1.41	256	2	7	1.4 * 10 <sup>6</sup>		
4	16	4	1	64	1	5	2 * 10 <sup>6</sup>		
5	32	4	1.41	128	2	5	2 * 10 <sup>6</sup>		
6	32	8	1.41	256	2	5	2 * 10 <sup>6</sup>		

No.	<u>H</u> J(plate) (A/m <sup>2</sup> ) Predict	<u>I</u> J(plate) Exptl @Vb	<u>J</u> J/p <sup>2</sup> Predict	<u>K</u> J/p <sup>2</sup> Exptl @Vb	<u>L</u> J(plate) (A/m <sup>2</sup> )	<u>M</u> J(plate) Exptl @max	<u>N</u> J/p <sup>2</sup> Predict	<u>O</u> J/p <sup>2</sup> Exptl @max
1	17.7	0	2.2 * 10 <sup>12</sup>	0	41.4	0	5.2 * 10 <sup>13</sup>	0
2	8.8	8.8	2.2 * 10 <sup>12</sup>	2.2 * 10 <sup>12</sup>	20.7	20.7	5.2 * 10 <sup>13</sup>	5.2 * 10 <sup>12</sup>
3	4.4	ND	2.2 * 10 <sup>12</sup>	ND	10.35	ND	5.2 * 10 <sup>12</sup>	ND
4	17.7	0	4.4 * 10 <sup>12</sup>	0	41.4	0	1.4 * 10 <sup>13</sup>	0
5	8.8	8.8	2.2 * 10 <sup>12</sup>	2.2 * 10 <sup>12</sup>	20.7	20.7	5.2 * 10 <sup>12</sup>	5.2 * 10 <sup>12</sup>
6	4.4	4.38	1.1 * 10 <sup>12</sup>	1.1 * 10 <sup>12</sup>	10.35	19.53	2.6 * 10 <sup>12</sup>	4.9 * 10 <sup>12</sup>

TABLE 2

<b>No.</b>	<b><u>A</u> Area (cm<sup>2</sup>)</b>	<b><u>B</u> I rms Input</b>	<b><u>C</u> <u>J</u> (plate) (A/m<sup>2</sup>)</b>
1	256	1.7	66.4
2	128	0.001	0.078
3	128	0.112	7.8
4	128	2.0	156.25
5	64	2.0	312.5
6	16	2.0	1,250
7	4	2.0	5,000

TABLE 3

No.	<u>A</u> Area (cm <sup>2</sup> )	<u>B</u> I rms Input (A)	<u>C</u> X- section area of plasma ball (cm <sup>2</sup> )	<u>D</u> Uncorr J (em) (A/m <sup>2</sup> )	<u>E</u> Method	<u>F</u> Emission area (cm <sup>2</sup> )	<u>G</u> J (em) (A/m <sup>2</sup> )	<u>H</u> Method
1	256	0.500	0.0333	$1.2 \times 10^5$	Videog; uncorr	$4.4 \times 10^{-4}$	$9 \times 10^6$	Videog; corr
2	128	0.119	0.0095	$1.25 \times 10^5$	Videog; uncorr	$1.3 \times 10^{-4}$	$9.5 \times 10^6$	Videog; corr
3	128	0.265	0.0177	$1.5 \times 10^5$	Videog; uncorr	$2.4 \times 10^{-4}$	$1.1 \times 10^7$	Videog; corr
4	128	0.500	0.038	$1.3 \times 10^5$	Videog; uncorr	$5.1 \times 10^{-4}$	$9.8 \times 10^6$	Videog; corr
5	128	1.030	0.0303	$3.4 \times 10^5$	Videog; uncorr	$4.4 \times 10^{-4}$	$2.6 \times 10^7$	Videog; corr
6	128	0.500	0.044	$1.1 \times 10^5$	NA	$5.9 \times 10^{-4}$	$8.5 \times 10^6$	Videog; corr
7	128	0.500	ND	NA	NA	$1.04 \times 10^{-4}$	$4.8 \times 10^7$	Metallog
8	128	0.100	ND	NA	NA	$3 \times 10^{-4}$	$3.3 \times 10^6$	Metallog
9	128	0.500	ND	NA	NA	$6.2 \times 10^{-4}$	$6.5 \times 10^6$	Metallog

TABLE 4

<b>No.</b>	<b>A</b> <b>Area</b> <b>(cm<sup>2</sup>)</b>	<b>B</b> <b>Gap</b> <b>(cm)</b>	<b>C</b> <b>Y<sub>b</sub></b> <b>(Volts)</b>	<b>D</b> <b>E @ Y<sub>b</sub></b> <b>(V/m)</b>	<b>E</b> <b>Torr</b>	<b>F</b> <b>Residual</b> <b>Gas</b>	<b>G</b> <b>Status</b>	<b>H</b> <b>Cathode</b> <b>material</b>
1	256	5	278	5,560	$2 \times 10^{-6}$	Ar	Sealed	H.Al.
2	128	5	774	15,480	$2 \times 10^{-6}$	Ar	Sealed	H.Al.
3	128	5	3500	70,000	$6 \times 10^{-4}$	Ar	Rotary Pump	H.Al.
4	128	5	1600	32,000	$9 \times 10^{-4}$	Ar	Rotary Pump	H.Al.
5	128	5	560	12,200	$4 \times 10^{-3}$	Ar	Rotary Pump	H.Al.
6	128	5	300	6,000	$8 \times 10^{-2}$	Ar	Rotary Pump	H.Al.
7	128	5.5	1350	24,545	$1 \times 10^{-3}$	Ar	Rotary Pump	H.Al.
8	16	4	560	14,000	$5 \times 10^{-2}$	Ar	Rotary Pump	H.Al.
9	4	8	560	7,000	$2 \times 10^{-1}$	Ar	Rotary Pump	H.Al.
10	10	9	900	10,000	$1 \times 10^{-4}$	Air	Sealed	Ni
11	10	18	1500	8,333	$1 \times 10^{-4}$	Air	Sealed	Ni

TABLE 5

<b>No.</b>	<b>A</b> <b>Volts</b>	<b>B</b> <b>Input</b> <b>Current</b> <b>(A)</b>	<b>C</b> <b>Pulse</b> <b>Time</b> <b>(msec)</b>	<b>D</b> <b>Input</b> <b>Energy</b> <b>per Pulse</b> <b>(Joules)</b>
1	3,500	0.010	0.5	$1.8 \times 10^{-2}$
2	1,020	0.001	1	$1 \times 10^{-3}$
3	600	0.100	6	$3.6 \times 10^{-1}$
4	560	0.500	20	5.60
5	560	1.700	3	2.85
6	560	1.700	30	28.56
7	560	1.200	48	32.26
8	560	4.000	50	112.00
9	250	0.500	80	10
10	250	1.100	20	5.5

TABLE 6

No	<u>A</u> Input Energy per pulse (Joules)	<u>B</u> Reactor Energy per pulse (Joules)	<u>C</u> Output Energy per pulse (Joules)	<u>D</u> PPS
1	0.1	0.3/0.5	0.16/0.2	60
2	0.33	1	1	60
3	0.38	2	2	60
4	1.84	ND	2.8	110
5	2	ND	121	0.2
6	4.3	ND	20.2	8
7	5.6	ND	154.5	0.2
8	6.5	367.7	353.8	0.2
9	8	71.5	25.2	1
10	14.4	ND	99	1
11	22.2	ND	72.9	0.8
12	26.8	ND	50	8
13	38.2	ND	80.3	1.5
14	44.8	261.5	253.5	0.3

TABLE 7

No.	<u>A</u> Current <i>i</i> in A	<u>B</u> <i>i</i> <sup>2</sup>	<u>C</u> <i>F<sub>R</sub></i> in dynes	<u>D</u> <i>ki</i> <sup>2</sup>	<u>E</u> <i>k</i>	<u>F</u> Proportionality	<u>G</u> Source
1	16	256	258.6	25,800	100.8	$10^2 i^2$	Tanberg
2	19	361	356.1	35,609	98.6	$10^2 i^2$	Tanberg
3	35	1,225	1,470	147,000	120	$10^2 i^2$	Kobel
4	12,700	$1.6 \times 10^8$	$0.9 \times 10^{10}$	$9.4 \times 10^{11}$	$5.8 \times 10^3$	$5 \times 10^3 i^2$	Graneau
5	25,400	$6.5 \times 10^8$	$4.3 \times 10^{10}$	$4.3 \times 10^{12}$	$6.6 \times 10^3$	$7 \times 10^3 i^2$	Graneau
6	1.6	2.56	143.6	14,359	$5.6 \times 10^3$	$6 \times 10^3 i^2$	PAGD
7	1.6	2.56	245.2	24,516	$9.6 \times 10^3$	$10^4 i^2$	PAGD

TABLE 8

<b>No.</b>	<b>A</b> <b>Element</b>	<b>B</b> <b>relative</b> <b>PAGD</b> <b>affinity</b>	<b>C</b> <b>Electro-</b> <b>negativity</b> $\chi=0.44\phi-0.15$	<b>D</b> <b>Work</b> <b>function <math>\phi</math></b> <b>(eV)</b>
1	Al	+++++	1.5	3.75
2	Zn	+++++	1.6	3.98
3	W	++++	1.7	4.20
4	Ni	++++	1.8	4.43
5	Fe	++++	1.8	4.43
6	Ag	+++	1.9	4.66
7	Cu	+	Cu(I) 1.9 Cu(II) 2.2	4.66 4.89

TABLE 9

Gas fill	Air, Nitrogen, Inert gas
Gas pressure, Torr	1 to $10^{-6}$
Interelectrode distance	2.0 to >20 cm
Electrode Geometry	Planar-parallel, hemi-cylindrical and co-axial
Cathode area	>2cm <sup>2</sup>
Electronegativity of cathode material	<1.0 to 2.2
Cathode work-function	<3.5 to 5.6 eV
Breakdown voltage	200 to 5,000 V
Breakdown fields	2,500 to >50,000
Current consumption	1 mA to >4A (in the PAGD regime)
Peak reactor current	1 mA to >250 A
Current density (cathode area)	0.05 to 5,000 A/m <sup>2</sup>
Current density (emission site) as a function of input power	$10^5$ to $5 * 10^7$ A/m <sup>2</sup>
PAGD rate	0.01 to >50,000 PPS
Duty cycle	1 to >40%
Pulse Time	0.1 msec to 100msec
Input energy per pulse	$10^{-3}$ to $>2 * 10^2$ J
Reaction energy per pulse (@ reactor)	<1 to $>5 * 10^2$ J
Reactor Dynamic Capacitance	100 $\mu$ F to >80 mF